The role of preferential diffusion on the ignition dynamics of lean premixed hydrogen flames

T. Yahou, N. Detomaso, Laurent Selle, Thierry Poinsot, J.R. Dawson, Thierry Schuller, D. Laera

Proceedings of the Combustion Institute 40 (2024) 105612

Contents lists available at ScienceDirect

Proceedings of the Combustion Institute

journal homepage: www.elsevier.com/locate/proci

The role of preferential diffusion on the ignition dynamics of lean premixed hydrogen flames

T. Yahou [a,b,*], N. Detomaso [c], L. Selle [b], T. Poinsot [b], J.R. Dawson [a], T. Schuller [b,e], D. Laera [d]

[a] Department of Energy and Process Engineering, Norwegian University of Science and Technology, Trondheim, Norway
[b] Institut de Mécanique des Fluides de Toulouse, IMFT, Université de Toulouse, CNRS, Toulouse, France
[c] CERFACS, 42 avenue Gaspard Coriolis, 31057 Toulouse, France
[d] Department of Mechanics, Mathematics and Management, Polytechnic University of Bari, Via Orabona, 70125, Italy
[e] Institut Universitaire de France (IUF), France

ARTICLE INFO

Keywords:
Ignition dynamics
Large-Eddy simulation
Hydrogen flame
Lewis number effects
Preferential diffusion effects

ABSTRACT

High-fidelity Large-Eddy Simulations (LES) are used to study the ignition dynamics of two fuel/air mixtures with distinct Lewis numbers Le, unveiling the impact of preferential diffusion during flame expansion including its stabilization above the burner. The simulations cover a CH_4/air mixture with a unity Lewis number $Le \approx 1$ and a lean H_2/air mixture with a sub-unity Lewis number $Le \approx 0.34$. Both mixtures are injected at a fixed bulk flow velocity of $U_b = 5$ m s^{-1}, with the equivalence ratio adjusted to match the laminar burning velocity $S_l^0 = 0.25$ m s^{-1}. LES results, including non-reacting flow velocity fields and ignition dynamics, are validated against a large experimental dataset encompassing non-reacting PIV, pressure overshoot, and flame visualization via OH-PLIF. This validation process significantly bolsters confidence in the chosen numerical approach. To elucidate the influence of preferential diffusion on flame propagation during the ignition process, the absolute flame speed is analyzed from kernel initiation, through complete consumption of the fresh gases to flame stabilization. It is found that despite having a lower thermal expansion ratio (ρ_u/ρ_b), the H_2/air flame still exhibits an enhanced absolute flame speed compared to the CH_4/air flame. This results in a similar pressure time-series over the full ignition process. An analysis isolating the effects of thermal expansion ratio and stretch effect reveals that this unexpected observation arises from the interplay between preferential diffusion, particularly evident in sub-unity Le mixtures, and the effects driven by the thermal expansion rate. Finally, the role of preferential diffusion and flame stretch on the local flame burning rate is investigated and it is demonstrated that LES can capture the effects of local enrichment observed in DNS studies.

1. Introduction

Hydrogen has emerged as a promising alternative to hydrocarbon fuels in gas turbines for propulsion, heat and power [1]. Yet, because of its extremely high reactivity and different combustion properties, widespread adoption of hydrogen (H_2) poses significant challenges in combustor design to ensure stability, operability and compliance with engine safety standards [2]. One of these challenges is the need to achieve secure and dependable ignition process across the widest possible range of operating conditions, while mitigating pressure overshoot and preventing flashback post-ignition [3,4].

Research into the ignition process has concentrated on unraveling fundamental aspects governing the flame dynamics at different times during the ignition sequence [5]. The ignition sequence is generally considered to occur over several phases, namely: kernel formation, flame propagation and flame stabilization. Studies into kernel development and flame propagation have so far pointed out the pivotal mechanisms that dictate the absolute flame propagation speed S_a of a growing flame [6]. In scenarios involving expanding flames in an initially quiescent flow, such as constant volume experiments [2], S_a scales with the unstretched laminar burning velocity S_l^0 propelled by the dilatation ratio, the ratio of the unburned to burned gas densities, (ρ_u/ρ_b) [7]. Studies on more realistic burners have emphasized the significant impact of flow dynamics, notably the effects of turbulence and shear layers, on the flame motion during ignition [8]. More recently, experimental studies on burner-to-burner flame propagation in annular combustors, have shown that in addition to the convection induced by the flow itself, the predominant driver of flame progression is the turbulent flame speed S_T rather than the laminar burning velocity S_l^0 [6,9]. These studies found that the light-round time is proportional

* Corresponding author at: Department of Energy and Process Engineering, Norwegian University of Science and Technology, Trondheim, Norway.
E-mail address: tarik.yahou@ntnu.no (T. Yahou).

https://doi.org/10.1016/j.proci.2024.105612
Received 4 December 2023; Accepted 5 July 2024
Available online 26 July 2024

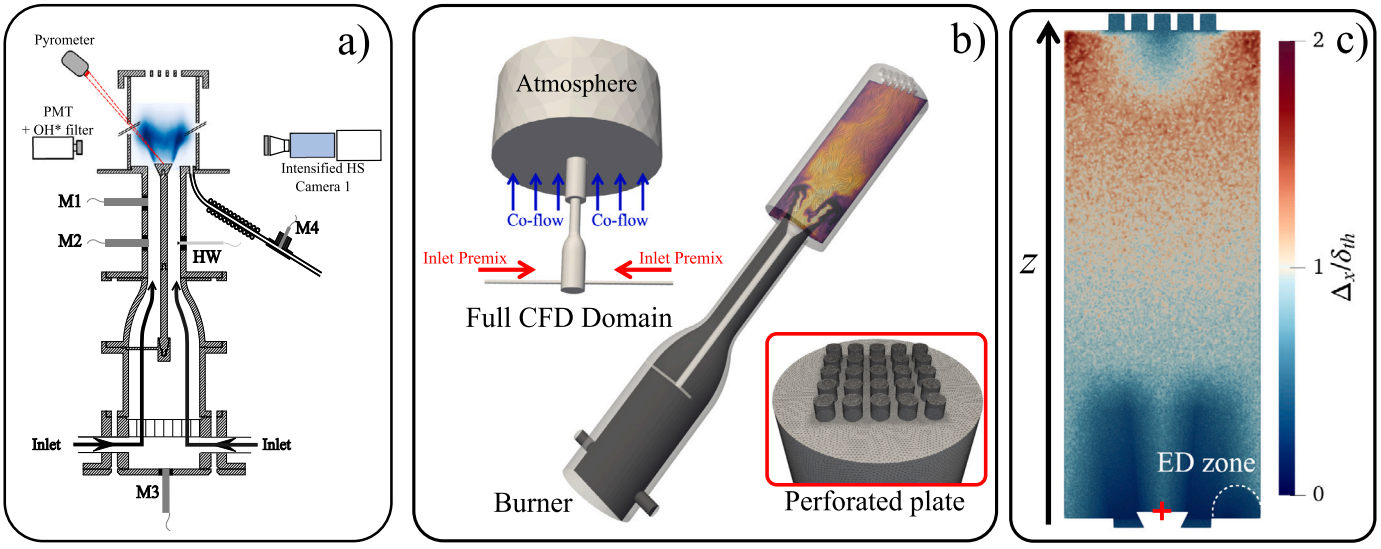

Fig. 1. (a) Schematic of the experimental setup with the main diagnostics. (b) LES computational domain. The full-length plenum and the perforated plate at the chamber outlet are taken into account. (c) Computational grid used inside the combustion chamber. The mesh size Δ_x is normalized by the minimum laminar flame thickness $\delta_{th} = 0.53$ mm of the cases considered in this study (see Table 1). In Fig. (c), the Energy Deposition (ED) zone where $\Delta_x = 60$ μm is highlighted by the white dashed line. The origin $z = 0$ mm, marked by the red marker, is set at the center of the bluff-body.

to $\Xi\left(\rho_u/\rho_b\right) S_l^0$, where $\Xi = A_T/A_0$ denotes the wrinkling factor that accounts for turbulence. The strong influence of the dilatation ratio and turbulence was also found in Large-Eddy Simulations (LES) of ignition and light-round with liquid spray flames [10,11].

Yet, the majority of these studies have predominantly centered around hydrocarbon fuels characterized by a unity Lewis number ($Le \approx 1$) which means that the flame is relatively insensitive to local variations in the stretch rate [12]. However, a feature of lean H_2 flames is its sub-unity Lewis number ($Le \ll 1$) which increases the flame sensitivity to stretch effects, further enhancing S_T [8]. Recent Direct Numerical Simulations (DNS) have quantified these local contributions to S_T by introducing a stretch factor I_0 [13–16]. For most conventional hydrocarbon fuels $I_0 = 1$ is observed, whereas above-unity values up to $I_0 = 4$ can be obtained for lean hydrogen mixtures [15]. These effects were suspected to significantly impact the ignition dynamics in both single-sector [4,17] and annular premixed combustors [18]. In these studies, S_l^0 was fixed for different CH_4/H_2 blends. Prior studies from Yahou et al. [4,17] showed that despite considerable variation in the volumetric expansion ratio $\left(\rho_u/\rho_b\right)$, all blends resulted in similar ignition pressure overshoot, suggesting uniform flame propagation speeds. Using the light around times to estimate the absolute flame speed S_a for different CH_4/H_2 blends, Kwah et al. [18] surprisingly found that S_a increases with decreasing $\left(\rho_u/\rho_b\right)$ and suggested that they may result from preferential diffusion effects.

These studies provided the first insight into the effect of hydrogen on ignition dynamics and showed that hydrogen results in distinctly different behaviors compared with conventional fuels. However, these studies were observational and unable to identify the fundamental mechanisms governing the different phases of the ignition sequence. To overcome these experimental limitations, high-fidelity LES are conducted to identify the underlying mechanisms that drive the ignition process of hydrogen flames.

2. Numerical setup and model

LES of the full ignition sequence are conducted on bluff body stabilized premixed flames as described in [17]. Fig. 1(a) displays a schematic of the atmospheric combustion rig along side with the main diagnostics. A perforated plate with 0.17 porosity is positioned at the outlet of the combustion chamber to increase the pressure drop and trigger flashback post-ignition. Further details regarding the burner geometry, the ignition system and measurement methods can be found in [4,17]. The ignition dynamics is investigated under perfectly premixed conditions with a constant bulk flow velocity and fixed laminar burning velocity. Two conditions are examined, a CH_4/air mixture at $\phi = 0.78$ and an H_2/air mixture at $\phi = 0.41$ to match $S_l^0 = 0.25$ m s^{-1}. In both scenarios, the bulk flow velocity is set at $U_b = 5$ m s^{-1}. Table 1 lists key combustion properties of the mixtures calculated at ambient temperature 300 K and 1 bar using complex transport in Cantera noting that the H_2/air flame has a lower thermal expansion ratio but an order of magnitude larger extinction strain rate.

Table 1
Operating conditions and laminar flame properties. Thermal flame thickness δ_{th} and volumetric expansion ratio $\sigma = T_b/T_u$ and extinction strain rate κ_{ext} computed using 1D Twin-Flame framework from CANTERA.

Flame	ϕ	δ_{th} [mm]	S_l^0 [m s^{-1}]	σ	κ_{ext} [s^{-1}]
CH_4/Air	0.78	0.53	0.25	6.7	900
H_2/Air	0.41	0.66	0.25	4.5	3150

The computational domain used for LES is shown in Fig. 1(b). The full length of the plenum as well as injection pipes are simulated to capture the flow dynamics after ignition and minimize the impact of the boundary conditions. The full domain including the perforated plate is discretized using an unstructured mesh which is refined until a grid-independent solution is obtained. The final mesh counts approximately 92 M tetrahedral elements. The grid has a characteristic size of $\Delta_x = 100$ μm arranged along the shear layer of the exiting jet. In the spark zone, the mesh is further refined to a characteristic size $\Delta_x = 60$ μm to ensure a minimum of 8 points within the flame thermal thickness [19] (see Fig. 1(c)). Simulations are performed using the high-fidelity compressible LES solver AVBP (www.cerfacs.fr/avbp7x/). The dynamic thickened flame model DTFLES [20] is used to resolve the flame on the LES grid and the sub-grid turbulent structures are accounted for by the Charlette model [21]. The convective terms are resolved using a third-order accurate Taylor–Galerkin finite-element scheme in both space and time [22]. Sub-grid turbulent scales are modeled using the SIGMA turbulent closure model [23].

Atmospheric pressure is imposed at the outlet of the domain using the Navier–Stokes Characteristic Boundary Conditions (NSCBC) formalism [24]. Inlet mass flow rates are controlled using the generalized non-reflecting boundary conditions NRI-NSCBC [25]. These conditions

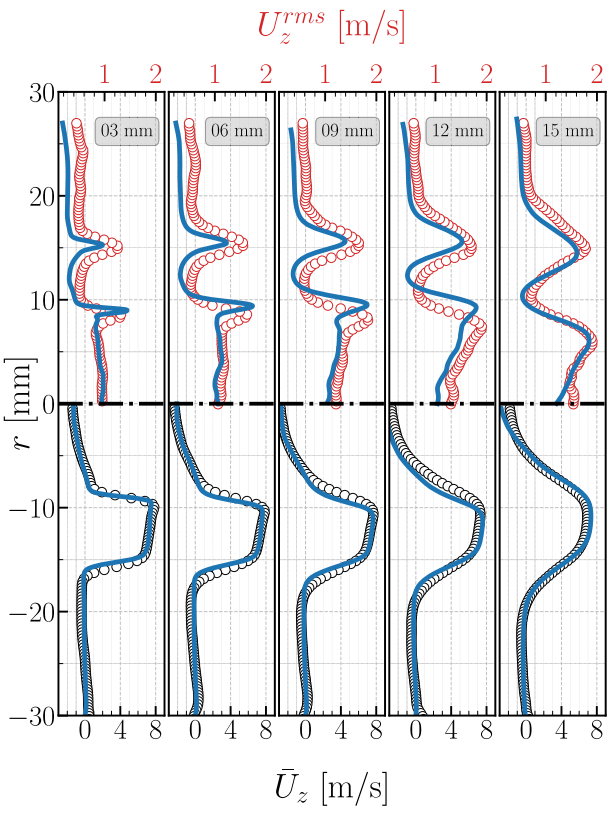

Fig. 2. Comparison of the mean $\bar{U}_z$ (bottom) and RMS U_z^{rms} (top) axial cold flow velocity profiles at five different locations above the injector. Markers denotes PIV data and solid blue line the LES results.

maintain the specified inlet velocities but permit acoustic fluctuations to leave the domain. The mixture conditions match the experiments (P = 1 bar and T_u = 300 K). The measured temperature of the bluff body is T_b = 470 K in the experiments, while T_w = 400 K is imposed for the rest of the chamber walls, including the perforated plate. Thermal losses on the walls are accounted for by applying a heat resistance of $R_w = 2.7 \times 10^{-3}$ W m^{2}K^{-1}, based on a thermal conductivity of λ = 1.47 W m^{-1}K^{-1} for a 4 mm thick quartz wall.

Ignition is simulated using the energy deposition (ED) model proposed in [26]. A Gaussian-distributed energy source term is applied in both time and space, centered 20 mm away from the burner axis (see Fig. 1(c)) and active between t = 0 ms and t = 0.6 ms. The total energy deposited matches the experimental spark energy of 36 mJ. Thanks to a high mesh resolution in the ED zone with Δ_x = 60 µm, the flame front is fully resolved to catch kernel formation and ensure that stretch effects on the flame propagation speed are well captured during the earliest stages of ignition sequence when the flame is highly curved. Far from this region, the thickened flame model is smoothly applied reaching a maximum F = 8 downstream of the region of interest, where stretch effects are less pronounced [27].

The methane chemical scheme relies on 2-Step BFER global mechanism [28], while hydrogen chemistry is modeled using the semi-detailed San Diego mechanism (9 species and 21 reactions) [29]. To account for preferential diffusion, species transport is modeled using simplified non-unity Lewis number approach for each species. As H_2 and air are perfectly premixed, this approach captures all preferential diffusion effects [16].

3. LES results and validation

3.1. Cold flow velocity fields

The non-reactive velocity fields from LES are initially compared with Particle Image Velocimetry (PIV) measurements obtained before ignition. Time-averages from LES are obtained over an entire flow-through time of the combustion chamber. Azimuthal averaging is conducted to mitigate any spatial dependencies in the flow field. Fig. 2 compares experimental (markers) and numerical (solid lines) mean streamwise velocity profiles, along with their corresponding RMS values at various heights z = 3, 6, 9, 12, and 15 mm above the injector. The results show very good agreement between LES and experimental data, accurately capturing both mean velocity $\bar{U}z$ and RMS fluctuations U_z^{rms}. This underlines the reliability of LES in predicting the shear layers, expansion angles, and turbulence levels. Additionally, the predicted total pressure drop ΔP_{LES} = 112 Pa across the system corresponding to pressure difference between the plenum and ambient conditions: $\Delta P = P_{M3} - P_{atm}$, corresponds to the measured value of ΔP_{exp} = 100 Pa.

3.2. Ignition overpressure and flame dynamics

LES and experiments are now compared during the ignition phase. It is worth noting for the entire ignition simulation cost is approximately 650 k CPUh for the CH4 case and about 720 k CPUh for the H2 case

A key indicator of a violent ignition process is the pressure overshoot relative to the mean value, which is plotted against time t in Fig. 3 for both CH_4 and H_2 flames. Pressure time-series are measured at M4 in Fig. 1(a). The average compiled over ten runs, i.e. ignition sequences performed for each operating condition is shown by the solid red line with its 'min–max' envelopes (shaded red). The corresponding pressure signals from LES are plotted in blue. The time, t = 0 ms, marks the

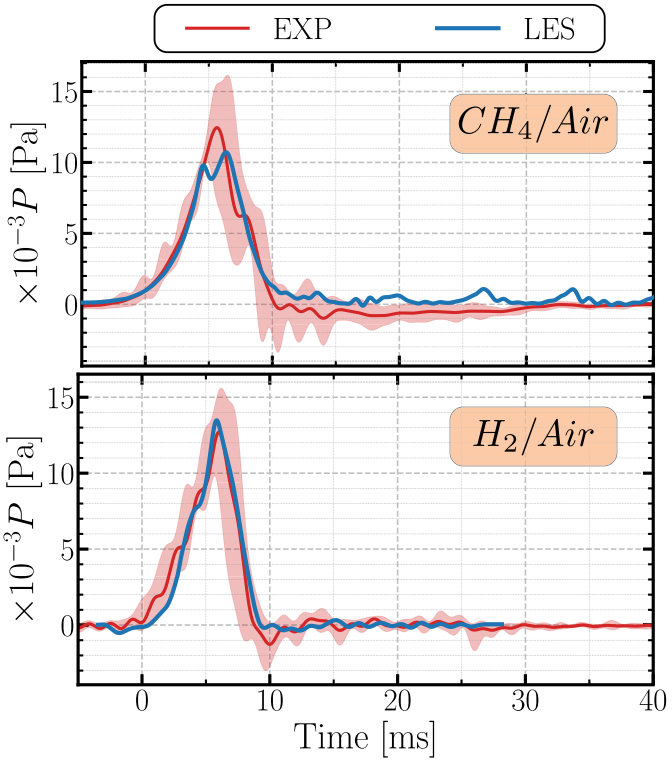

Fig. 3. Time-series of the chamber pressure during ignition. The blue solid line denotes the LES results and red solid line the measurements averaged over 10 runs. The red shaded region corresponds to the 'min–max' envelope.

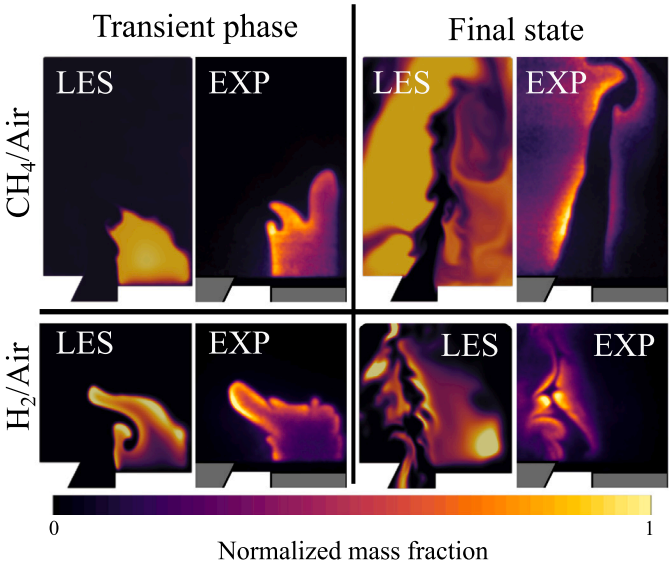

Fig. 4. Direct flame comparison between OH-PLIF against LES Y_{OH} and Y_{CO_2} mass fraction for H_2 and CH_4 flames, respectively. Two instants representing transient flame ignition and final state are shown. Data are normalized by their maximum value for each flame.

appearance of the first flame kernel. For both operating conditions, the LES shows excellent agreement with the experiments capturing both the ignition time and the amplitude of the pressure impulse, 12 kPa and 14 kPa for CH_4 and H_2 flames respectively. Despite the transient nature of the ignition process, the numerical results consistently fall within the experimental uncertainties with a deviation in the amplitude lower than 10%. It is noted that in the CH_4 case the LES slightly underestimates the peak amplitude and leads to a larger disparity between the predicted peak pressures of CH_4 and H_2 flames of ±4 kPa, compared with ±2 kPa from the measurements.

A qualitative comparison of flame dynamics during ignition is presented in Fig. 4. It shows OH Planar Laser Induced Fluorescence OH-PLIF measurements synchronized with numerical fields of Y_{OH} for H_2 and Y_{CO_2} for CH_4 flames. The LES successfully predicts the main features of the flame as it interacts with the jet shear layer. Due to its lower extinction limit, the CH_4 flame is quenched near the injector lip in correspondence with the high strained region of the flow (see Fig. 2)

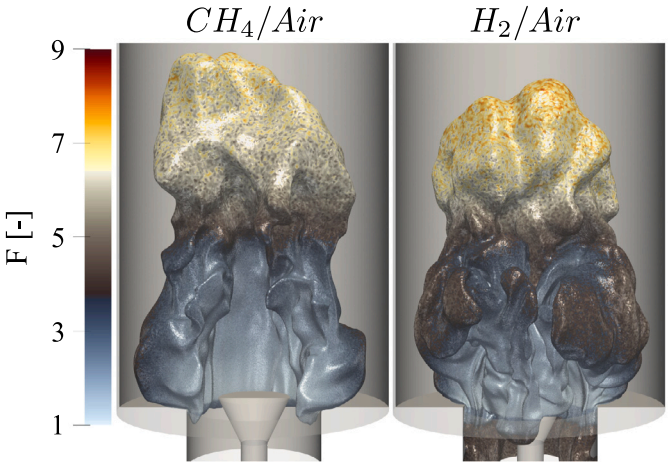

Fig. 5. Variations in the flame thickening factor F for the CH_4/Air (left) and H_2/Air (right) flames.

whereas the high extinction strain rate of the H_2 flame allows it propagate through the main jet. Furthermore, the simulations successfully capture the final stabilization states for each fuel. The CH_4/air flame is stabilized on the bluff-body whereas the H_2/air experiences flashback. The good agreement between LES and experiments demonstrates the robustness of the selected numerical approach.

Fig. 5 shows the 3D flame structure represented by an isosurface of progress variable $c = 1 - (Y_f/Y_f^{in}) = 0.85$ (where Y_f and Y_f^{in} refers to the local and inlet fuel mass fraction, respectively color-coded by the thickening factor F. Near the injector outlet, where high strain rates occur, both flames feature a restricted thickening factor $F \leq 3$, facilitated by a refined grid in this zone (see Fig. 1(c)). This refinement minimizes the influence of non-resolved sub-grid scales, preserving the Lewis number effects on the flame burning rate [27]. Far from this region, the flame curvature reduces and larger thickening factors $3 \leq F \leq 8$ are applied. This approach boosts confidence in the numerical simulations by minimizing modeling uncertainties in determining the flame speed, specifically when the flame front is highly curved. It is important to note that the primary aim of this study is to provide insights into the ignition dynamics of lean hydrogen flames. A fundamental investigation of the preferential diffusion effects is beyond the scope of this work and would require highly resolved Direct Numerical Simulations (DNS) [14–16,30].

4. Flame propagation

4.1. Absolute turbulent flame speed

In the following, the flame dynamics during ignition is scrutinized by focusing on the absolute flame propagation speed S_a which is a significant factor in determining the magnitude of the pressure impulse after ignition [17]. Within this study, S_a is computed during the expansion phase of the initial flame kernel. As illustrated in Fig. 4, the flame takes on an arch-like topology propagating toward the chamber exit. The instant when the flame front reaches the outlet marks the end of the expansion phase which is characterized here by the time-scale when the Heat Release Rate (HRR) reaches its maximum. Throughout this flame expansion phase, an expression for the resolved absolute turbulent flame speed S_a^{res}, i.e, the absolute flame velocity over the resolved flame surface, can be derived by considering the rate of change in the volume of burnt gas as follows [11]:

$$S_a^{res} = \frac{1}{\langle A_T \rangle} \frac{d\langle V_b \rangle}{dt} \tag{1}$$

where $\langle V_b \rangle$ and $\langle A_T \rangle = \int_V |\nabla c| \, dV$ denote the resolved burnt gas volume and the resolved flame surface area, respectively. Both can be measured in the LES. The normalized time evolution of S_a^{res} for the two

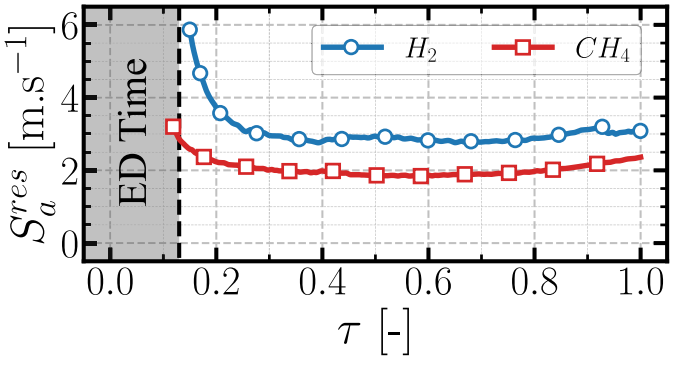

Fig. 6. Time evolution of absolute turbulent flame speed S_a^{res} over the resolved flame surface computed with Eq. (1). The gray shaded region denotes the energy deposition period where the gases are not yet ignited. Time is normalized by t_{HRR}.

fuel mixtures is depicted in Fig. 6 where $\tau = t/t_{HRR}$. The figure shows that following the energy deposition time (gray shaded zone), the initial flame kernel initially propagates at $S_a^{res} = 6.0$ and 3.5 m s^{-1} for H_2 and CH_4 flames, respectively. The enhancement of S_a^{res} for H_2 is notably stronger than for CH_4. Shortly after, S_a^{res} quickly reaches a steady value close to 3 m s^{-1} for H_2 and 2.0 m s^{-1} for CH_4 throughout the entire expansion phase. Although Table 1 shows that the CH_4/air flame has a greater volumetric expansion ratio, $(\rho_u/\rho_b)\, S_l^0 = 1.7$ m s^{-1}, than the H_2/air flame, $(\rho_u/\rho_b)\, S_l^0 = 1.2$ m s^{-1}, the H_2/air flame exhibits a marginally higher propagation speed in Fig. 6. This difference in flame speed likely accounts for the observed difference in the peak pressure impulse observed in Fig. 3. These findings indicate that lean H_2/air mixtures do not follow the conventional expectation of a direct correlation between flame propagation speed and expansion ratio observed in conventional hydrocarbon fuels [6,9,31]. The unique combustion properties of lean H_2/air flames, characterized by strong preferential diffusion, makes the flame more susceptible to stretch effects which enhances the burning rate and compensates for the reduced thermal expansion ratio.

4.2. Impact of volumetric expansion and stretch

To investigate this latter point, it is instructive to quantify the impact of the volumetric expansion ratio and the stretch effects on the flame propagation speed. The mean stretch factor I_0 averaged over the entire flame surface which accounts for all local variations in the flame structure is evaluated from LES using the relation proposed in [13]:

$$I_0 = \frac{\Omega^*}{S_l^0}\frac{1}{A_T} \tag{2}$$

where

$$\Omega^* = -\frac{\int_V \rho \dot{Y}_f dV}{\rho_u Y_f^{in}} \tag{3}$$

is the normalized total burning rate (m^3 s^{-1}) over the total volume V, $\dot{Y}_f$ (s^{-1}) is the fuel source term and Y_f^{in} the fuel mass fraction.

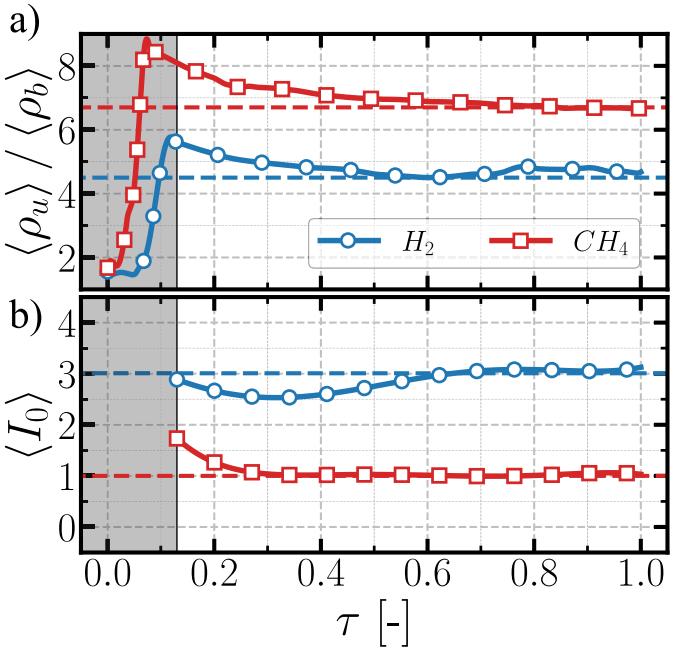

Fig. 7. (a) Volumetric expansion ratio: Solid lines denote LES resolved signal and the dashed lines the values obtained from 1D flame simulation. (b) Stretch factor I_0 computed from Eq. (2).

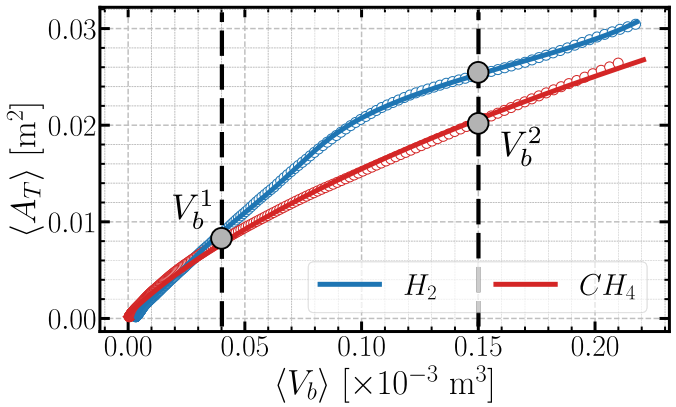

Fig. 8. Resolved turbulent flame surface area $\langle A_T\rangle$ plotted against the burnt gas volume $\langle V_b\rangle$.

The temporal evolution of ρ_u/ρ_b and the stretch factor I_0 during the expansion phase are plotted in Fig. 7(a,b). The results show that soon after ignition both the expansion ratios and stretch factors stabilize, maintaining constant values throughout the entire expansion phase for both fuel mixtures. As anticipated from 1D simulations, a higher thermal expansion ratio is evident for the CH_4/air flame where $\rho_u/\rho_b \simeq 6.7$ compared to $\rho_u/\rho_b \simeq 4.5$ for the H_2/air flame. Interestingly, the opposite trend is observed for the stretch factor I_0. In the case of CH_4/air mixture with $Le \approx 1$, I_0 stabilizes at a value of 1.0 as expected whereas the lean H_2/air mixture reaches a super-unity value of approximately $I_0 = 3.0$. This discrepancy underscores the pronounced influence of stretch on the propagation speed of the H_2 flame which compensates for any reduction in the thermal expansion ratio compared to the CH_4 flame.

In these carefully selected conditions, where the cold flow field and turbulence levels are consistent across both mixtures, the ratio between velocity fluctuations u' and the turbulent integral length scale l_t remains constant in both cases ($u'/l_t = cst$). In addition to the fixed laminar burning velocity S_l^0, the 1D thermal thickness δ_{th} of both flames differ by less than 8%. Hence, it is reasonable to assume that the flame-turbulence interaction, characterized by the Damköhler number $Da = S_l^0 l_t/u'\delta_{th}$, is comparable for both mixtures. As a consequence, the observed difference in the value of I_0 can therefore be attributed predominantly to thermodiffusive effects of lean premixed H_2/air mixtures with $Le \ll 1$.

5. Effect of preferential diffusion

5.1. Flame surface comparison

This section delves into the impact of preferential diffusion by examining the flame dynamics throughout the expansion phase. To illustrate this, Fig. 8 plots the evolution of the turbulent flame surface area $\langle A_T\rangle$ against the burnt gas volume $\langle V_b\rangle$. For small burnt gas volumes, $\langle V_b\rangle \leq V_b^1 = 0.04 \times 10^{-3}$ m^3, both flames have similar surface areas. However, as the flames grow and produce larger burnt gas volumes $\langle V_b^2\rangle$, the H_2/air flame exhibits a larger flame surface area for the same burnt gas volume. For example, when $\langle V_b\rangle = V_b^2 = 0.15 \times 10^{-3}$ m^3 in Fig. 8, the CH_4/air flame has a surface area $\langle A_T\rangle = 200$ cm^2 whereas the H_2/air flame shows a total flame surface area $\langle A_T\rangle = 250$ cm^2.

The increase in $\langle A_T\rangle$ between H_2 and CH_4 is a direct consequence of preferential diffusion effects which leads to more corrugated flame surface [14–16,30]. This is confirmed by comparing the two flames in Fig. 9 which shows snapshots of the 3D isocontour at $c = 0.85$ taken at the burnt gas volume labeled V_b^2 in Fig. 8. It is worth noting that the sub-grid model is the same for both CH_4 and H_2 case, and therefore these thermodiffusive effects manifest within the resolved scales of the LES. Models including preferential diffusion effects at the sub-grid scale [32,33] are not used in the present simulations.

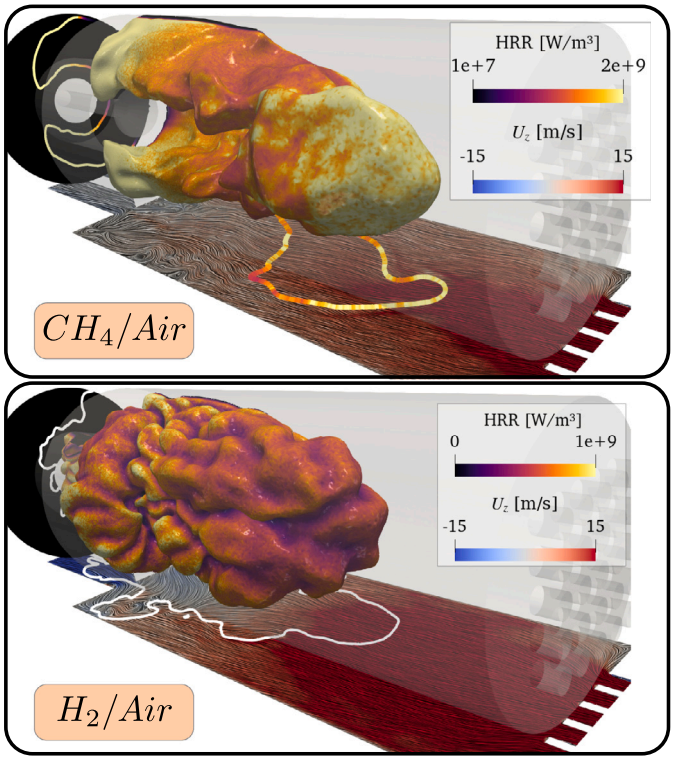

Fig. 9. Direct 3D flame visualization. The flame is represented by an iso-surface of progress variable at $c = 0.85$, color-coded by the Heat Release Rate (HRR). The axial velocity in the central plane is also shown. (For interpretation of the references to color in this figure legend, the reader is referred to the web version of this article.)

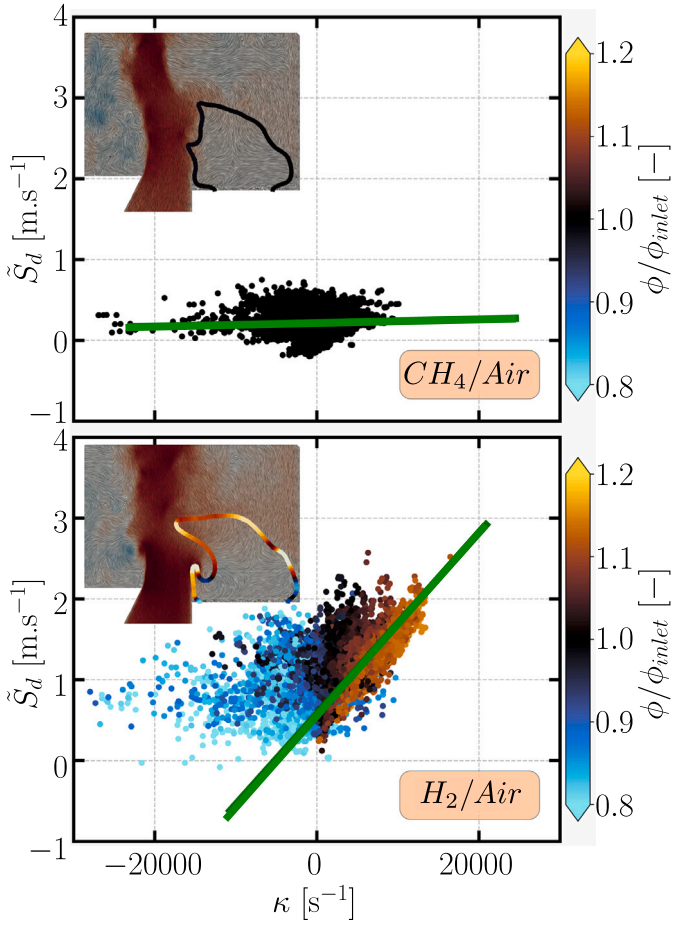

Fig. 10. Scatter plots of the reduced flame displacement speed $\tilde{S}_d$ with respect to the total stretch κ, computed along the iso-surface $c = 0.85$. Data correspond to point V_b^1 in Fig. 8. Scatter plots are colored by local equivalence ratio ϕ/ϕ_{in}. (For interpretation of the references to color in this figure legend, the reader is referred to the web version of this article.)

5.2. Flame displacement speed analysis

To further elucidate the underlying mechanisms driving the divergence in the evolution of flame surface area with respect to burnt gas volume for $V_b > V_b^1$ in Fig. 8, the density-weighted flame displacement speed $\tilde{S}_d = (\rho/\rho_u) S_d$ is locally analyzed in Fig. 10, which displays a scatter plot distribution of $\tilde{S}_d$, color-coded by the normalized local equivalence ratio ϕ/ϕ_{in}, with respect to total flame stretch κ [34]:

$$\kappa = -\mathbf{nn} : \nabla\mathbf{u} + \nabla \cdot \mathbf{u} + S_d (\nabla \cdot \mathbf{n}) \quad (4)$$

where $\mathbf{n}$ and $\mathbf{u}$ represent the flame normal and the flow velocity, respectively. All variables are computed at iso-surface $c = 0.85$ of the progress variable.

For the CH_4/air flame, consistent with theoretical expectations, $\tilde{S}_d$ is barely affected by flame stretch with the scatter distribution close to a constant value around $\tilde{S}_d \approx 0.3$ m s^{-1}. This trend is highlighted by a linear regression (solid green line), computed by solely considering points exhibiting positive stretch. As expected for a unity Lewis number combustible mixtures, all flame elements maintain a uniform equivalence ratio of $\phi/\phi_{in} = 1$, regardless of variations in κ.

Conversely, for the lean H_2/air flame, $\tilde{S}_d$ increases with the flame stretch. For the majority of the flame elements with low stretch values $\kappa \leq 500$ s^{-1}, $\tilde{S}_d$ remains approximately similar to the values observed for the CH_4/air case between $0.2 \leq \tilde{S}_d \leq 0.5$ m s^{-1}. However, for highly stretched flame elements, $\tilde{S}_d$ exceeds 2.0 m s^{-1} in Fig. 10, emphasizing the substantial impact of preferential diffusion on the flame response to stretch, thereby enhancing the flame burning rate. Moreover, variations in the local equivalence ratio relative to the inlet value value ϕ_{in} are evident. Flame elements experiencing negative stretch, under compression, demonstrate local ϕ lower than the inlet value ($\phi/\phi_{\text{in}} < 1$), whereas those subjected to positive stretch exhibit values exceeding unity ($\phi/\phi_{in} > 1$) increasing the local flame speed. These locally enriched areas correspond to flame cusps convexly curved towards the fresh gas, as highlighted from the slice view in Fig. 10 and observed in previous DNS studies [14–16].

6. Conclusion

High-fidelity LES has been used to reveal the impact of preferential diffusion on ignition dynamics of premixed flames. CH_4 and H_2 fuel/air mixtures injected with uniform bulk flow velocity have been considered. The equivalence ratio was varied to match the laminar unstretched burning velocity for both mixtures. The numerical approach was validated against experimental data, including comparison of the velocity field, flame dynamics and ignition timing and unsteady pressure are successfully captured through the entire ignition sequence.

LES post-processed results has been used to complement the experiments and identify the mechanisms driving flame propagation during the expansion phase. Unexpectedly, despite its lower thermal expansion ratio ρ_u/ρ_b, the hydrogen/air flame exhibits a higher absolute flame speed S_a^{res} compared to the methane/air mixture. This is attributed to the interplay between thermal expansion and stretch effects evaluated via the stretch factor I_0. While the CH_4/air flame has a higher thermal expansion ratio, the H_2/air flame displays higher I_0 values due to preferential diffusion. Analyzing the local flame dynamics revealed a uniform density-weighted flame displacement speed $\tilde{S}_d = (\rho/\rho_b) S_d$ for the CH_4/air flame. However, for the H_2/air flame, a strong correlation

between $\tilde{S}_d$ and stretch κ emerges indicating that preferential diffusion has a significant impact on the local flame response by creating regions of local enrichment along the flame front that accelerate the flame propagation.

Novelty and significance statement

The primary novelty of this work lies in its exploration of the impact of preferential diffusion on the ignition dynamics of lean premixed flames. Large-Eddy Simulations were conducted across the entire ignition sequence of CH4/air and H2/air mixtures, each characterized by distinct Lewis numbers. These simulations aimed to complement previous experimental observations, revealing the underlying mechanisms inaccessible through experiments, including thermal expansion, flame stretch, and local enrichment. These findings carry practical implications for the design of next-generation H2-combustion systems, highlighting the pivotal role of preferential diffusion in H2 flame ignition. Finally, our study underscores the capability of LES to capture these effects when approached methodically, showcasing its potential in comprehending intricate hydrogen combustion dynamics. This understanding could significantly aid in optimizing the design of H2-combustion technologies.

CRediT authorship contribution statement

T. Yahou: Designed research, Performed experiments, Performed simulations, Analyzed data, Wrote the paper. **N. Detomaso:** Designed research, Performed simulations, Analyzed data, Reviewed the paper. **L. Selle:** Reviewed simulation, Reviewed data. **T. Poinsot:** Reviewed data, Reviewed the paper. **J.R. Dawson:** Designed research, Reviewed the data, Reviewed the paper. **T. Schuller:** Designed research, Analyzed data, Reviewed the data, Reviewed the paper. **D. Laera:** Designed research, Analyzed data, Reviewed data, Reviewed the paper.

Declaration of competing interest

The authors declare that they have no known competing financial interests or personal relationships that could have appeared to influence the work reported in this paper.

Acknowledgments

This work was supported by the NCCS Centre (FME Grant 257579/E20) and received HPC resources from EuroHPC PRACE project No. EHPC-REG-2023R01-140 (I-MODERN). Special thanks to Dr. G Staffelbach for assistance with the HPC.

References

[1] M. Stefanizzi, T. Capurso, G. Filomeno, M. Torresi, G. Pascazio, Recent combustion strategies in gas turbines for propulsion and power generation toward a zero-emissions future: Fuels, burners, and combustion techniques, Energies 14 (20) (2021) 6694.
[2] C.K. Law, G. Jomaas, J.K. Bechtold, Cellular instabilities of expanding hydrogen/propane spherical flames at elevated pressures: theory and experiment, Proc. Combust. Inst. 30 (1) (2005) 159–167.
[3] M. Fischer, Safety aspects of hydrogen combustion in hydrogen energy systems, Int. J. Hydrogen Energy 11 (9) (1986) 593–601.
[4] T. Yahou, T. Schuller, J.R. Dawson, The effect of ignition procedure on flashback of hydrogen-enriched flames, J. Eng. Gas Turbines Power 146 (1) (2023).
[5] A.H. Lefebvre, D.R. Ballal, Gas Turbine Combustion: Alternative Fuels and Emissions, CRC Press, 2010.
[6] J.-F. Bourgouin, D. Durox, T. Schuller, J. Beaunier, S. Candel, Ignition dynamics of an annular combustor equipped with multiple swirling injectors, Combust. Flame 160 (8) (2013) 1398–1413.
[7] G.R. Ruetsch, J.E. Broadwell, Effects of confinement on partially premixed flames, Annu. Res. Briefs 1995 (1995).
[8] J.F. Driscoll, Turbulent premixed combustion: Flamelet structure and its effect on turbulent burning velocities, Prog. Energy Combust. Sci. 34 (1) (2008) 91–134.
[9] R. Ciardiello, P.M. de Oliveira, A.W. Skiba, E. Mastorakos, P.M. Allison, Effect of spark location and laminar flame speed on the ignition transient of a premixed annular combustor, Combust. Flame 221 (2020) 296–310.
[10] K. Töpperwien, S. Puggelli, R. Vicquelin, Analysis of flame propagation mechanisms during light-round in an annular spray flame combustor: the impact of wall heat transfer and two-phase flow, Combust. Flame 241 (2022) 112105.
[11] S. Puggelli, D. Veynante, R. Vicquelin, Impact of dynamic modelling of the flame subgrid scale wrinkling in large-Eddy simulation of light-round in an annular combustor, Combust. Flame 230 (2021) 111416.
[12] G. Damköhler, Der einfluss der turbulenz auf die flammengeschwindigkeit in gasgemischen, Z. Elektrochem. Angew. Phys. Chemie 46 (11) (1940) 601–626.
[13] A. Attili, S. Luca, D. Denker, F. Bisetti, H. Pitsch, Turbulent flame speed and reaction layer thickening in premixed jet flames at constant Karlovitz and increasing Reynolds numbers, Proc. Combust. Inst. 38 (2) (2021) 2939–2947.
[14] L. Berger, A. Attili, H. Pitsch, Synergistic interactions of thermodiffusive instabilities and turbulence in lean hydrogen flames, Combust. Flame 244 (2022) 112254.
[15] M. Rieth, A. Gruber, F.A. Williams, J.H. Chen, Enhanced burning rates in hydrogen-enriched turbulent premixed flames by diffusion of molecular and atomic hydrogen, Combust. Flame 239 (2022) 111740.
[16] V. Coulon, J. Gaucherand, V. Xing, D. Laera, C. Lapeyre, T. Poinsot, Direct numerical simulations of methane, ammonia-hydrogen and hydrogen turbulent premixed flames, Combust. Flame 256 (2023) 112933.
[17] T. Yahou, J. Dawson, T. Schuller, Impact of chamber back pressure on the ignition dynamics of hydrogen enriched premixed flames, Proc. Combust. Inst. 39 (4) (2023).
[18] Y.H. Kwah, S. Wiseman, J. Dawson, The effect of methane-ammonia and methane-hydrogen blends on ignition and light-around in an annular combustor, J. Eng. Gas Turbines Power 145 (11) (2023) 1–12.
[19] B. Rochette, F. Collin-Bastiani, L. Gicquel, O. Vermorel, D. Veynante, T. Poinsot, Influence of chemical schemes, numerical method and dynamic turbulent combustion modeling on LES of premixed turbulent flames, Combust. Flame 191 (2018) 417–430.
[20] J.-P. Legier, T. Poinsot, D. Veynante, Dynamically thickened flame LES model for premixed and non-premixed turbulent combustion, in: Proc. Summer Progr., Vol. 12, Citeseer, 2000, pp. 157–168.
[21] F. Charlette, C. Meneveau, D. Veynante, A power-law flame wrinkling model for LES of premixed turbulent combustion Part I: non-dynamic formulation and initial tests, Combust. Flame 131 (1–2) (2002) 159–180.
[22] O. Colin, M. Rudgyard, Development of high-order Taylor–Galerkin schemes for LES, J. Comput. Phys. 162 (2) (2000) 338–371.
[23] F. Nicoud, H.B. Toda, O. Cabrit, S. Bose, J. Lee, Using singular values to build a subgrid-scale model for large Eddy simulations, Phys. Fluids 23 (8) (2011).
[24] T.J. Poinsot, S.K. Lele, Boundary conditions for direct simulations of compressible viscous flows, J. Comput. Phys. 101 (1) (1992) 104–129.
[25] G. Daviller, G. Oztarlik, T. Poinsot, A generalized non-reflecting inlet boundary condition for steady and forced compressible flows with injection of vortical and acoustic waves, Comput. & Fluids 190 (2019) 503–513.
[26] G. Lacaze, E. Richardson, T. Poinsot, Large eddy simulation of spark ignition in a turbulent methane jet, Combust. Flame 156 (10) (2009) 1993–2009.
[27] N. Detomaso, J.-J. Hok, O. Dounia, D. Laera, T. Poinsot, A generalization of the Thickened Flame model for stretched flames, Combust. Flame 258 (2023) 113080.
[28] B. Franzelli, E. Riber, L.Y.M. Gicquel, T. Poinsot, Large eddy simulation of combustion instabilities in a lean partially premixed swirled flame, Combust. Flame 159 (2) (2012) 621–637.
[29] P. Saxena, F.A. Williams, Testing a small detailed chemical-kinetic mechanism for the combustion of hydrogen and carbon monoxide, Combust. Flame 145 (1–2) (2006) 316–323.
[30] A.J. Aspden, M.S. Day, J.B. Bell, Characterization of low Lewis number flames, Proc. Combust. Inst. 33 (1) (2011) 1463–1471.
[31] D. Barré, L. Esclapez, M. Cordier, E. Riber, B. Cuenot, G. Staffelbach, B. Renou, A. Vandel, L.Y.M. Gicquel, G. Cabot, Flame propagation in aeronautical swirled multi-burners: Experimental and numerical investigation, Combust. Flame 161 (9) (2014) 2387–2405.
[32] T.L. Howarth, A.J. Aspden, An empirical characteristic scaling model for freely-propagating lean premixed hydrogen flames, Combust. Flame 237 (2022) 111805.
[33] A. Aniello, D. Laera, L. Berger, A. Attili, T. Poinsot, Introducing thermodiffusive effects in large-eddy simulation of turbulent combustion for lean hydrogen-air flames, in: Proc. Summer Progr. 2022, CTR, 2022.
[34] S.M. Candel, T.J. Poinsot, Flame stretch and the balance equation for the flame area, Combust. Sci. Technol. 70 (1–3) (1990) 1–15.